Synergistic Effect of Ferroptosis-Inducing Nanoparticles and X-Ray Irradiation Combination Therapy

Chaewon Bae, Rodrigo Hernández Millares, Suhyun Ryu, Hyowon Moon, Dongwoo Kim, Gyubok Lee, Zhuomin Jiang, Min Hee Park, Kyung Hwan Kim, Woong Sub Koom,* Sung-Joon Ye,* and Kangwon Lee*

Ferroptosis, characterized by the induction of cell death via lipid peroxidation, has been actively studied over the last few years and has shown the potential to improve the efficacy of cancer nanomedicine in an iron-dependent manner. Radiation therapy, a common treatment method, has limitations as a stand-alone treatment due to radiation resistance and safety as it affects even normal tissues. Although ferroptosis-inducing drugs help alleviate radiation resistance, there are no safe ferroptosis-inducing drugs that can be considered for clinical application and are still in the research stage. Here, the effectiveness of combined treatment with radiotherapy with Fe and hyaluronic acid-based nanoparticles (FHA-NPs) to directly induce ferroptosis, considering the clinical applications is reported. Through the induction of ferroptosis by FHA-NPs and apoptosis by X-ray irradiation, the therapeutic efficiency of cancer is greatly improved both in vitro and in vivo. In addition, Monte Carlo simulations are performed to assess the physical interactions of the X-rays with the iron-oxide nanoparticle. The study provides a deeper understanding of the synergistic effect of ferroptosis and X-ray irradiation combination therapy. Furthermore, the study can serve as a valuable reference for elucidating the role and mechanisms of ferroptosis in radiation therapy.

1. Introduction

Cancer nanomedicine has been a potential and promising treatment approach for cancer for many years.[1–4] Nanoparticles are designed to target tumors, enhance drug delivery, and improve therapeutic efficacy; however, safety concerns, such as toxicity and side effects, have hampered their clinical application, and thus, nanoparticles are a reality that has yet to reach its full potential.[5–7] In addition, complete cancer cell death is difficult to achieve as these cells exhibit resistance to existing therapies because of the heterogeneity of tumors and the tumor microenvironment.[8,9] In fact, in anticancer clinical practice, the treatment effect is maximized through various combination treatments rather than monotherapy; therefore, continuous research on various combination therapies is needed.[10,11]

In nanomedicine, cancer cell death is generally induced through apoptotic and

C. Bae
Program in Nanoscience and Technology
Graduate School of Convergence Science and Technology
Seoul National University
Seoul 08826, Republic of Korea
R. Hernández Millares
Program in Biomedical Radiation Sciences
Department of Transdisciplinary Studies
Graduate School of Convergence Science and Technology
Seoul National University
Seoul 08826, Republic of Korea
S. Ryu, D. Kim, G. Lee, Z. Jiang, S.-J. Ye, K. Lee
Department of Applied Bioengineering
Graduate School of Convergence Science and Technology
Seoul National University
Seoul 08826, Republic of Korea
E-mail: sye@snu.ac.kr; kangwonlee@snu.ac.kr

M. H. Park
THEDONEE
1208, 156, Gwanggyo-ro, Yeongtong-gu, Suwon-si, Gyeonggi-do 16506, Republic of Korea
H. Moon, K. H. Kim, W. S. Koom
Department of Radiation Oncology
Yonsei Cancer Center
Heavy Ion Therapy Research Institute
Yonsei University College of Medicine
Seoul 03722, Republic of Korea
E-mail: mdgold@yuhs.ac
S.-J. Ye
Biomedical Research Institute
Seoul National University Hospital
Seoul 03080, South Korea
S.-J. Ye
Advanced Institute of Convergence Technology
Seoul National University
Suwon 16229, South Korea
S.-J. Ye, K. Lee
Research Institute for Convergence Science
Seoul National University
Seoul 08826, Republic of Korea

necroptotic cell death, among other cell death mechanisms; however, the discovery of ferroptosis in 2012,[12] has prompted active studies of the possibility of the treatment of cancer using nanomedicine and ferroptosis. Unlike other forms of programmed cell death, such as apoptosis and necrosis, ferroptosis is a type of cell death in which reactive oxygen species (ROS) and hydroperoxide accumulate via an iron-induced reaction, with lipid peroxidation eventually occurring in sequence. Although iron is essential for cell-cycle regulation, cell proliferation, and DNA synthesis, it is also a target for cancer treatment[13–15] because, unlike normal cells, cancer cells display significant differences in iron metabolism, such as the upregulation of iron-absorption proteins, transferrin receptor 1 (TFR1), and the downregulation of iron-efflux proteins, ferroportin, in the degree of the net iron influx.[16,17] Because of the significant alteration of iron metabolism observed exclusively in cancer cells, ferroptosis, which is a type of cell death based on iron metabolism, is attracting attention in the field of anticancer treatment. Therefore, to develop a treatment through ferroptosis in cancer nanomedicine, research on the possibility and performance of anticancer treatment using nanoparticles, as well as research on the mechanism of ferroptosis are continuously and actively being reported.[18–23]

In clinical cancer treatment, X-rays are a commonly and widely used radiation therapy and have remained one of the standard cancer treatments for decades because of their good effectiveness. In fact, 50% of cancer patients receive radiation therapy, and even though it is the cornerstone of cancer treatment, complete response to cancer treatment is still challenging due to radiation resistance, remarking the necessity for radiosensitizers.[24] In addition, X-ray irradiation kills cancer cells by inducing a cell death mechanism based on DNA damage, mainly via an apoptosis mechanism.[25,26] Many studies have reported synergistic effects between X-ray therapy and the use of nanoparticles in cancer nanomedicine. Recently, the interest in combining ferroptosis and X-ray irradiation has been increasing as a potential strategy to improve the therapeutic effect of cancer therapies;[27–29] if the mechanism of ferroptosis and the apoptosis triggered by X-rays are induced at the same time, a higher anticancer effect can be expected, such as the death of cancer cells that had exhibited treatment resistance or avoidance. For this reason, ferroptosis inducers (FINs) have been used as radiosensitizers. Nevertheless, most of the FINs used in combination with radiation therapy haven't been approved or are underway to be tested clinically as they are poorly tolerated in vivo or even have toxic side effects. Therefore, nano-based platforms have been proposed as a way to tackle FIN-associated drawbacks.[30–32] However, beyond the consequential aspect, showing that the combination treatment using nanoparticles and radiation therapy had a synergistic effect, unveiling the mechanisms underlying the synergistic effect of nanoparticles combined with radiation treatment is of great importance. A few studies have proposed ferroptosis-inducing nanoparticles in combination with ionizing radiation, nevertheless, they are still far from actual clinical application.[33–36] Monte Carlo simulations are a valuable tool to simulate the behavior of complex systems, such as the interaction between ionizing radiation and materials that are commonly used in cancer therapy.[37–40] We can accurately predict the radial dose distributions around nanoparticles, which may provide valuable insights into the physical means of the combination of nanoparticles with ionizing radiation.

We examined the effect of combination therapy using X-ray irradiation with hyaluronic acid-based nanoparticles with Fe (FHA-NPs), which are safe particles that induce ferroptotic cell death that were previously reported in detail elsewhere regarding their clinical application (**Figure 1**).[18] We observed a correlation between the experimental results and those of the Monte Carlo simulations. FHA-NPs are internalized through the high affinity between HA and the ligand of the CD44, cancer overexpression receptor; followed by degradation by hyaluronidase in lysosomes, the generation of lipid ROS, and, finally the ferroptotic cell death via lipid peroxidation. In addition, DNA is damaged through X-ray irradiation, ROS accumulates in mitochondria, and apoptotic cell death is induced. Through MC simulations, we investigated the interaction between low-energy X-rays (e.g., 300 kVp) and the FHA-NPs, and observed a dose enhancement in their close vicinity. We confirmed the improved therapeutic effect of the combination treatment in vitro and in vivo and demonstrated a correlation between the improved tumor treatment effect and the combination treatment. This work may be used as a reference for developing a combination therapy strategy with an improved anticancer therapeutic effect via the combination of ferroptosis-inducing nanoparticles and X-ray irradiation, followed by the characterization of the role of ferroptosis in this process.

2. Results and Discussion

2.1. Effect of FHA-NPs and X-Ray Irradiation on Cell Viability

To confirm the ability of A549 and A375P cells to proliferate and form colonies after treatment, the cell viability of the FHA-NP, X-ray irradiation, and combined treatment (FHA-NP + X-ray) treatment groups were compared through clonogenic assays, which are generally used to determine cell proliferation and survival after irradiation.[41–43] The clonogenic assay was performed in triplicate for each experimental group. Individual colonies were visualized by crystal violet staining, and significant colony formation inhibition was confirmed even when FHA-NPs were administered alone; moreover, a higher X-ray irradiation dose resulted in a stronger colony formation inhibitory effect in A549 (**Figure 2A**; Figure S1, Supporting Information) and A375P cells (Figure 2B; Figure S2, Supporting Information). Compared with the control (Ctrl) group, we confirmed the observation of a significant inhibitory effect on colony formation in the group treated with 200 μg mL^{-1} FHA-NPs alone, the group treated with X-ray irradiation at 1, 3, and 6 Gy, and the group treated with the combination regimen. After irradiation with 6 Gy, the observed colony-reduction rate in the A549 cell was 55.8% and 63.2%, respectively, compared to the control group and the FHA-NP-treated cells. Similarly, the reduction rate in A375P cells after 6 Gy irradiation was 84.4% and 88.6% compared to the control group and the FHA-NPs treated cells, respectively. For all experimental doses (1, 3, and 6 Gy), the surviving fraction (SF) of A549 and A375P cells treated with FHA-NPs was significantly lower than that of the Ctrl group. In addition, the calculated sensitizer enhancement ratio (SER) were 1.07 and 1.12 for A549 and A375P, respectively, which demonstrated a sensitizing effect for the FHA-NPs. Figure 2C,E depicts the clonogenic SF of A549 and A375P cells after irradiation with 300 kVp X-rays with and without FHA-NP administration. The curves were fitted with a linear quadratic model, i.e.,
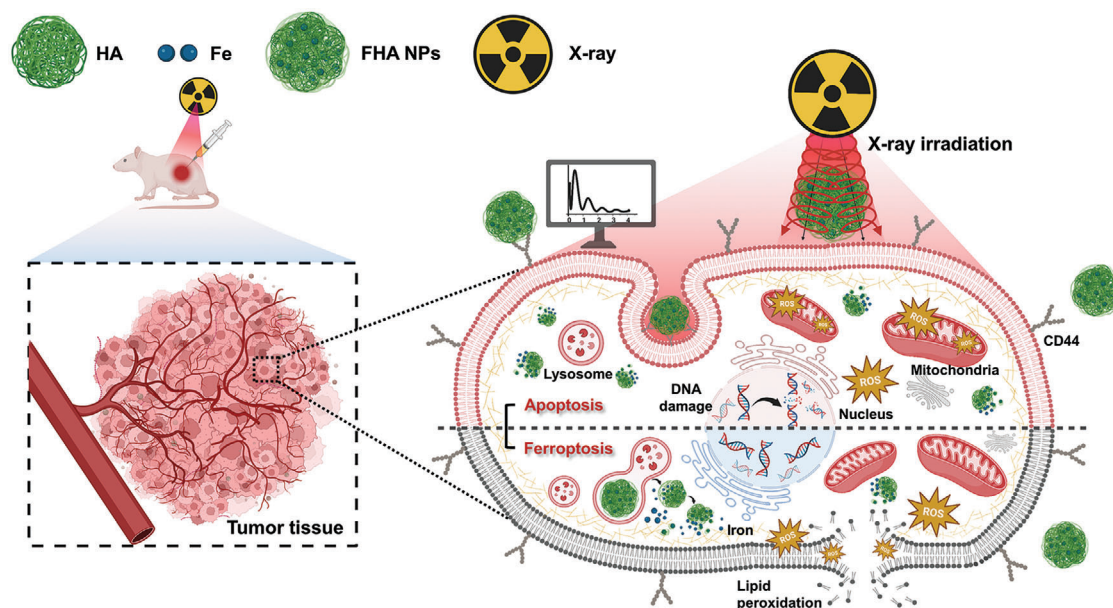
ADVANCED
SCIENCE NEWS
www.advancedsciencenews.com

NANO · MICRO
small
www.small-journal.com

Figure 1. Schematic illustration of the combination therapy system of FHA-NPs and X-ray irradiation for tumor therapy: Combination therapy of ferroptotic cell death through FHA-NPs, which induce lipid peroxidation, and apoptotic cell death by X-rays, which cause DNA damage, and improvement of X-ray sensitivity by FHA-NPs.

survival $= e^{-\alpha D - \beta D2}$. The α and β parameters obtained together with the SER are reported in Figure 2D,F. The major impact of the treatment with FHA-NPs was on the α parameter, which is typically related to the direct effects of ionizing radiation on DNA. The obtained SERs values of 1.07 and 1.12 suggest a slightly enhanced radiation effect caused by the FHA-NPs. The SER reports the effect of the radiation on the colony formation leaving aside the ferroptosis effect induced by the FHA-NPs. The nanoparticles enhanced the radiation lethality, meaning the radiation and FHA-NPs effect do not act separately but also in conjunction as a radiosensitizer.

Next, we examined the activity of lactate dehydrogenase (LDH), which is a cytosolic enzyme that is released upon damage to the cell membrane.[44] We observed that the LDH activity was significantly higher in the combination treatment, with the activity being higher in the order of the FHA-NP treatment group followed by the X-ray irradiation group. In A549 cells, LDH activity was more than twofold higher in the FHA-NP-treated group versus the group treated with X-ray irradiation alone (Figure 2G). In A375P cells, we confirmed that it was higher in the FHA-NPs-treated group than in the X-ray-only group and that the increase was much more significant in the combination treatment group (Figure 2H). The characteristic of FHA-NPs, which induce ferroptotic cell death through lipid peroxidation, may be considered to be related to LDH activity. We additionally confirmed the valence state of Fe in FHA-NPs through XPS because the presence of Fe^{2+} and Fe^{3+} affects inducing ferroptosis. High-resolution Fe 2p spectra of FHA-NPs showed spin-orbit doublet peaks of Fe $2p_{3/2}$ and Fe $2p_{1/2}$. As a result of analyzing FHA-NPs, the binding energies of Fe $2p_{3/2}$ and $2p_{1/2}$ were measured to be 710.54 and 722.92, respectively, indicating that Fe^{2+} and Fe^{3+} exist in FHA-NPs (Figure S3, Supporting Information). We also performed live/dead analysis to evaluate cell viability in A549 (Figure 2I,

Figure S4, Supporting Information) and A375P cells (Figure 2J; Figure S5, Supporting Information) during ferroptosis-induced FHA-NP, X-ray irradiation, and combination treatments. The ratio of dead cells recorded at 12 h after X-ray irradiation was higher in the FHA-NP-treated group than it was in the X-ray irradiation group; furthermore, viable cells were almost non-existent in the combination treatment group both A549 and A375P cells. We verified the cancer cell-killing abilities of FHA-NPs and X-ray irradiation, respectively, and confirmed a significant synergy effect through the improved cancer cell-killing effect in combination therapy.

2.2. Enhancement of the Radiation Effect After FHA-NP Treatment In Vitro

As reported previously, FHA-NPs induce ferroptosis. Here, we assessed the mechanism of cell death induced by X-ray irradiation. First, we performed a TUNEL assay after treatment with FHA-NPs or X-ray at 6 Gy, separately or simultaneously in A549 cells (**Figure 3A**). The green color indicates TUNEL staining, whereas the red color represents the counterstaining of the cytoskeleton with phalloidin and the blue color represents the counterstaining of the nucleus. As shown in Figure 3B, we quantified the TUNEL-positive fluorescence intensity, which was hardly observed after the treatment with FHA-NPs but was significantly increased after irradiation with X-rays; furthermore, the fluorescence intensity was further improved after the combination treatment. In the TUNEL assay, which evaluates the DNA fragmentation damage, in contrast with the FHA-NP treatment, a fluorescence signal was observed exclusively under X-ray irradiation, indicating that a different cell death mechanism was induced by the FHA-NP and X-ray treatments. In the evaluation
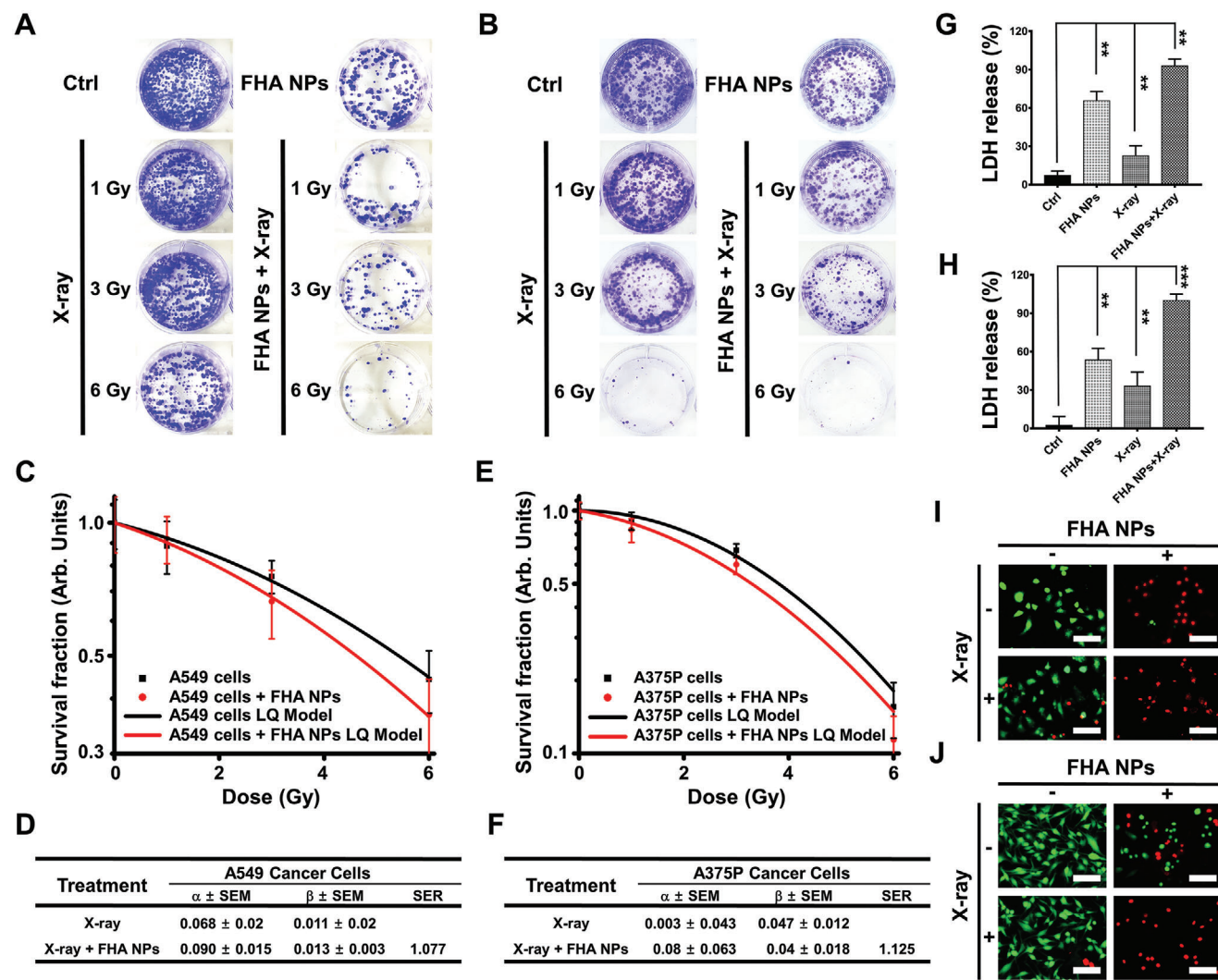
Figure 2. Therapeutical effect of FHA-NPs in combination with X-ray irradiation in A549 and A375P cells. Image of the clonogenic analysis of A) A549 and B) A375P cells after X-ray irradiation at 1, 3, and 6 Gy depending on whether FHA-NPs were administered or not. C) Survival fraction and curve fitting of A549 cells treated with and without FHA-NPs. D) Linear quadratic model parameters (α and β) and calculated SER extracted by curve fitting of the clonogenic-assay-derived survival fractions at 0, 1, 3, and 6 Gy in A549 cells. E) Survival fraction and curve fitting of A375P cells treated with and without FHA-NPs. F) Linear quadratic model parameters (α and β) and calculated SER extracted by curve fitting of the clonogenic-assay-derived survival fractions at 0, 1, 3, and 6 Gy in A375P cells. Lactate dehydrogenase activity in G) A549 and H) A375P cells upon single and combined treatment with FHA-NPs and X-ray irradiation. Data are presented as the mean ± SD for five replicates, $^{**}p < 0.01$, $^{***}p < 0.001$. Live/dead assay after treatment with FHA-NPs and X-ray irradiation, simultaneously or separately in I) A549 and J) A375P cells. Green and red colors represent live and dead cells, respectively (scale bar, 100 µm).

of the results of TUNEL staining, which continues to be widely used as a measure of apoptotic cell death by labeling the free 3′-hydroxyl termini and detecting DNA breakage,[45,46] a clear difference was observed only in the X-ray-irradiated group. In turn, in the group treated with FHA-NPs, which induces ferroptosis, almost no fluorescence was observed, whereas apoptotic cell death was induced after irradiation with X-rays. We then performed a Comet assay to assess the radiation-induced DNA damage in A549 (Figure 3C) and A375P cells (Figure 3D). The DNA damage was measured based on the tail moment, tail length, and percentage of DNA in the tail, and a graph was prepared based on the average of 50 cells in A549 (Figure 3E; Figures S6 and S7, Supporting Information) and A375P cells (Figure 3F; Figure S8, Supporting Information).

porting Information). In A549 cells, the tail moment value was 44.2% ± 9.9% after treatment with X-rays alone, and increased to 64.6% ± 13.6% after treatment with FHA-NPs together with X-ray, compared with the almost null value obtained in the case of the Ctrl and FHA-NP treatment alone. Consistent with the results of the TUNEL analysis, almost no DNA damage was observed after treatment with FHA-NPs, whereas the DNA damage increased after X-ray irradiation and reached a maximum after the combined treatment. In A375P cells, the tail moment value was 32.6% ± 11.8% after treatment with X-rays alone and increased to 46.6% ± 13.5% after treatment with FHA-NPs together with X-rays. These results suggest that the DNA damage caused by X-ray irradiation increased when this modality was combined
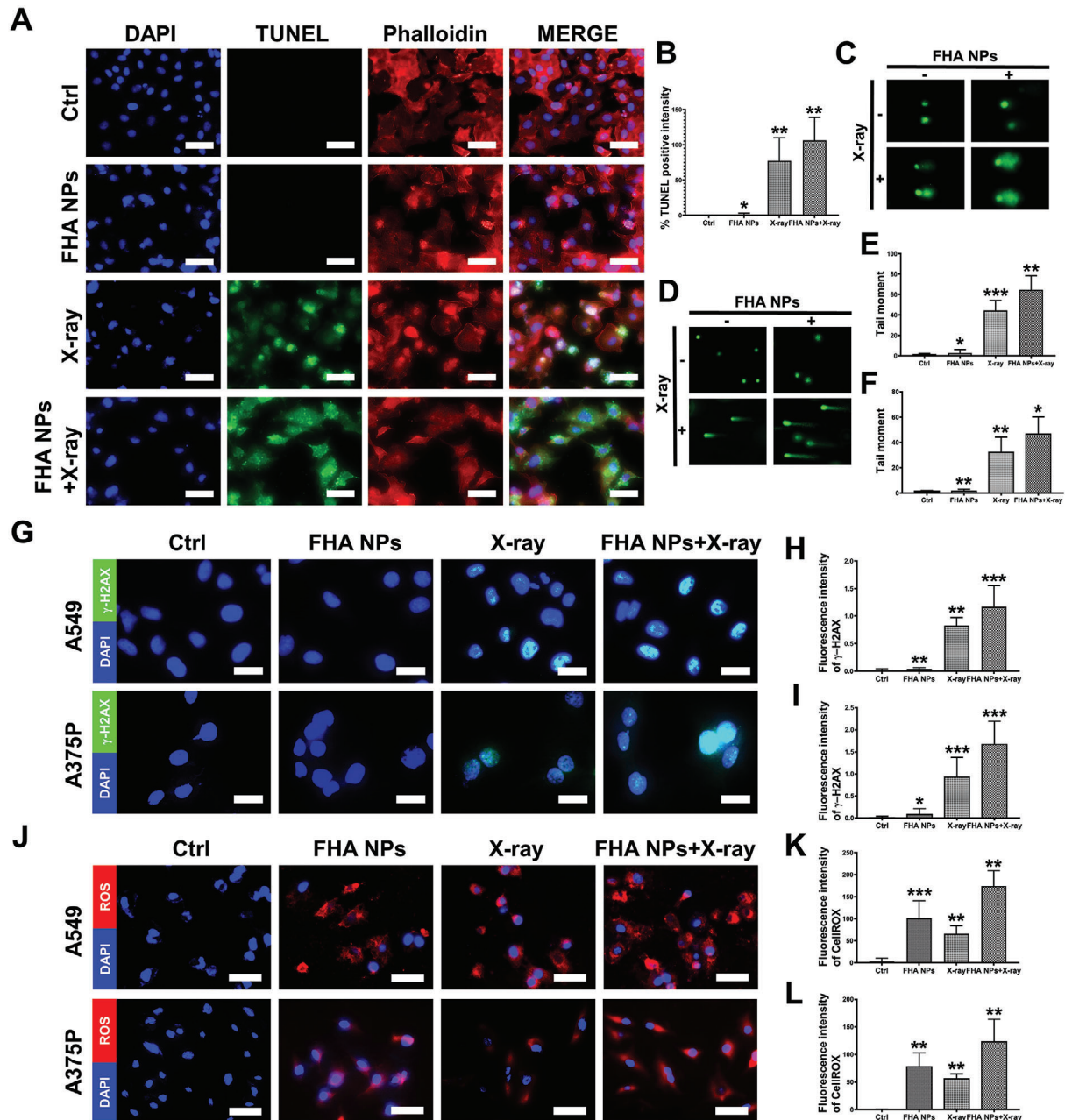
**ADVANCED
SCIENCE NEWS**

www.advancedsciencenews.com

NANO · MICRO
small

www.small-journal.com

Figure 3. Confirmation of an enhanced radiation effect after FHA-NP treatment in vitro. A) TUNEL staining after treatment with FHA-NPs or X-ray irradiation, separately or simultaneously. Blue, green, and red colors represent nuclear, TUNEL, and phalloidin staining (scale bar, 50 μm). B) Graph for the quantification of the TUNEL-positive fluorescence intensity. Data are presented as the mean ± SD. Comet assay results after treatment with FHA-NPs or X-ray irradiation, separately or simultaneously in C) A549 and D) A375P cells. Graph of the tail moment in the presence and absence of FHA-NPs and X-ray irradiation in E) A549 and F) A375P cells. G) Fluorescence intensity of γ-H2AX foci in A549 and A375P cells. Blue and green colors indicate nuclear and H2A staining, respectively (scale bar, 25 μm). Graph for the quantification of the fluorescence intensity of γ-H2AX foci in H) A549 and I) A375P cells. J) Images of DAPI and CellROX Orange showing ROS generation after separate or simultaneous treatment with FHA-NPs and X-ray irradiation in A549 and A375P cells. Blue and red represent nuclear and ROS (scale bar, 50 μm). Graph for the quantification of the fluorescence intensity of CellROX Orange in K) A549 and L) A375P cells. *$p < 0.05$, **$p < 0.01$, ***$p < 0.001$.

with FHA-NP treatment, compared with X-ray irradiation alone, and the combination treatment had an amplifying effect on A549 and A375P cell death.

Next, as shown in Figure 3G, the DNA damage induced by FHA-NPs and X-ray irradiation, together or separately, was in-

vestigated regarding the formation of γ-H2AX foci, which were counted and quantified in A549 (Figure 3H) and A375P cells (Figure 3I). Compared with X-ray irradiation alone, the number of γ-H2AX foci was low in both A549 and A375P cells in the group treated with FHA-NPs alone; however, the combination of

ADVANCED
SCIENCE NEWS

www.advancedsciencenews.com

NANO · MICRO

small

www.small-journal.com

FHA-NPs with X-ray irradiation yielded a higher percentage of γ-H2AX foci in A549 (Figure S9, Supporting Information) and A375P cells (Figure S10, Supporting Information). In A549 cells, the fluorescence intensity of γ-H2A was 0.01 ± 0.03 in the control group and 0.03 ± 0.02 in the FHA-NPs group and increased significantly to 0.82 ± 0.15 after irradiation with X-rays and to 1.17 ± 0.38 in the combination treatment. And, in A375P cells, the fluorescence intensity of γ-H2A was 0.01 ± 0.13 in the control group and 0.1 ± 0.12 in the FHA-NPs group and increased significantly to 0.93 ± 0.52 after irradiation with X-rays and to 1.68 ± 0.57 in the combination group. Irradiation alone induced the formation of nuclear γ-H2AX foci, whereas the combined treatment markedly increased the number of nuclear γ-H2AX foci. Our data indicate that the number of γ-H2AX foci was significantly increased upon co-treatment with FHA-NPs and irradiation. Overall, FHA-NPs potentiated the X-ray-induced DNA damage in vitro, suggesting that A549 and A375P cells may become more sensitive to radiation through the exacerbation of DNA damage. As shown in Figure 3J, the level of ROS was assessed in A549 and A375P cells using CellROX after separate or simultaneous treatment with FHA-NPs and X-rays. The level of ROS increased both when FHA-NPs were administered alone and when X-rays were irradiated alone. Compared with the Ctrl group (without any treatment) of A549 cells, the fluorescence intensity increased to 101 ± 39.2 when FHA-NPs alone were administered, to 65.4 ± 18.2 when X-ray irradiation alone was delivered, and to 173.9 ± 34.7 after the combined treatment (Figure S11, Supporting Information; Figure 3K). In the A375P cell group, the fluorescence intensity increased to 78.6 ± 24.3 when FHA-NPs were administered alone, to 49.2 ± 11.8 when administered with X-ray alone, and to 129.9 ± 44.2 when combined treatment was administered (Figure S12, Supporting Information; Figure 3L). A higher level of ROS expression was observed after treatment with FHA-NPs alone versus X-ray irradiation alone; moreover, the ROS expression level increased significantly after the administration of the combined treatment. Thus, we verified that the level of ROS was induced to a much greater extent by FHA-NPs compared with X-ray irradiation and confirmed that the combined treatment yielded synergistic effects. The expression of ROS is a very important feature that is commonly observed in both ferroptosis and X-ray irradiation-induced apoptosis. Referring to previous studies, FHA-NPs, which induce ferroptosis, appear to accumulate lipid ROS mainly via iron[47–49] and to accumulate ROS in mitochondria after irradiation with X-rays.[50,51] Although the degree of expression was different, we demonstrated that ROS were significantly expressed in the cases of both FHA-NPs and X-ray irradiation. Based on these results, we consider that further studies of the location of ROS expression and the correlation and mechanism of ROS expression through other pathways are needed.

2.3. Confirmation of Biodistribution by Optical Diffraction Tomography

Optical diffraction tomography (ODT) combined with fluorescence images was used to assess the FHA-NP uptake and its effect on cell morphology in A549 cells. **Figure 4A** is a 2D refractive index (RI) tomography image and Figure S13 (Supporting Information) is a 2D RI Nanolive image confirmed after treatment of FHA-NPs and X-rays separately or simultaneously, and Figure 4B is a fluorescence image confirmed after staining the nucleus and mitochondria with DAPI and mitotracker, respectively. As can be seen in the enlarged image at the bottom of the square box, the difference in mitochondrial morphologies was observed. As previously reported, both ferroptosis and X-ray irradiation induce morphological changes and directly affect the mitochondria. Previous literature has established that as ferroptosis progresses, mitochondrial contraction, membrane rupture, and fragmentation occur.[52,53] Similarly, X-ray irradiation is known to cause mitochondrial swelling, fragmentation, and membrane potential change.[54,55] In fact, significant differences in mitochondria were observed in all groups treated with FHA-NPs, X-rays, and combination treatment compared to the Ctrl group. We observed small and disconnected mitochondria in both the FHA-NPs and X-ray groups. In addition, in the group treated with combined treatment, the fluorescence sensitivity of mitochondria was significantly lowered and a significant amount of round shapes were observed beyond the disconnected sites. In the cross-sectional slices of 3D RI tomograms, we can see the intracellular structures along with a large number of FHA-NPs internalized for NP-treated cells (Figure 4C).

Next, we confirmed the RI values and indicated holotomography via color labeling. The RI values for the A549 cell line of the cytoplasm and the nucleus were found to be in the range of 1.34–1.35 and 1.35–3.36, respectively. Values in the range 1.37–1.38 were attributed to lipid droplets or cytoplasmic lysosomes, and values higher than 1.38 were assumed to be FHA-NPs. The intracellular localization of FHA-NPs, cellular nuclei, cytoplasm, and lipid droplets is shown in Figure 4D. In the rendered 3D refractive index distribution image, blue and white represent the nucleus and cytoplasm, yellow represents lipid droplets or cytoplasmic lysosomes, and red represents FHA-NPs. We made a rather noteworthy finding here. In the group treated with FHA-NPs alone and in combination with X-ray, we observed that yellow color, representing lipid droplets or cytoplasmic lysosomes, was expressed much, and some surrounded red color, representing FHA-NPs. In the Ctrl group without any treatment, the yellow color was hardly confirmed, whereas in the group irradiated with X-rays, some confirmation was observed, but we observed that it was more concentrated near the nucleus. We consider it worth noting the significantly higher amount of lipid droplets/cytoplasmic lysosomes for the NP-treated cells, which can be directly related to the cellular response to the FHA-NPs.

Afterward, we performed quantitative analysis of the tomographic images by deep-learning-based segmentation algorithms by the Tomoanalysis software (Figures 4E–L; S8–S11, Supporting Information). Figure 4E,F represent the mean RI and sphericity of A549 whole cells. The mean RI was higher in the group treated with FHA-NPs, and in sphericity, which is a measure of how spherical the cells are, the sphericity caused by cell death was the smallest in the combination treatment. Since apoptosis, a death caused by X-ray irradiation, and the nucleus correlate, we identified the mean RI, sphericity, surface area, and volume of the nucleus and nucleolus (Figures S14–S17, Supporting Information). In terms of the mean RI and sphericity, there were minor differences in the nucleus and the nucleolus; on the contrary, in terms of surface area
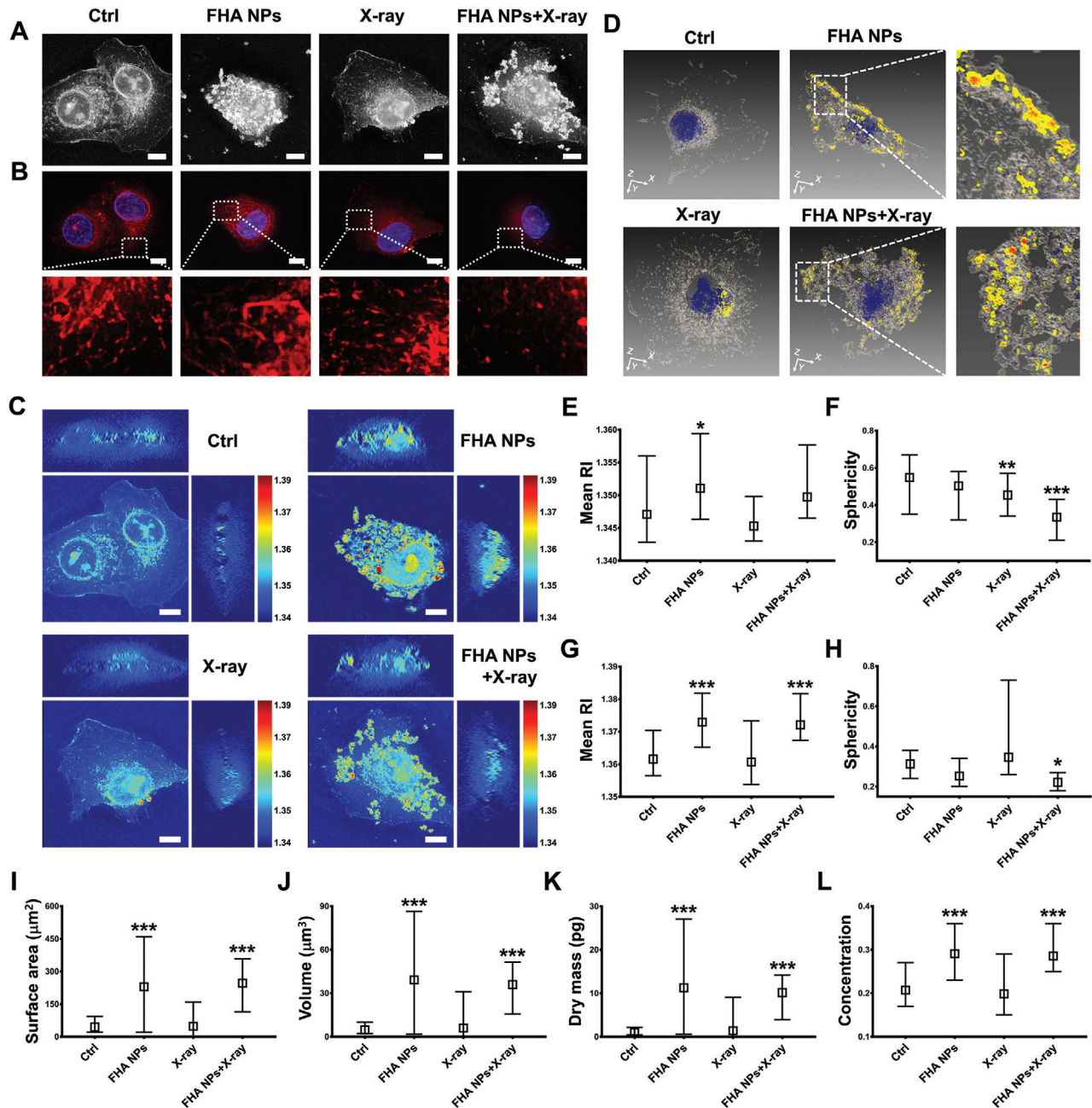
ADVANCED
SCIENCE NEWS

www.advancedsciencenews.com

NANO · MICRO
small
www.small-journal.com

Figure 4. Confirmation of biodistribution based on the 3D refractive index. A) Images of individual or co-treatment groups for FHA-NPs and X-ray irradiation (scale bar, 9 μm). B) Fluorescence image of nuclear staining with DAPI and mitochondrial staining with MitoTracker. An enlarged image is provided at the bottom (scale bar, 9 μm). C) Sectional slices of 3D refractive index tomogram after single or simultaneous treatment of FHA-NPs and X-ray in A549 cells. Values in the color bar represent refractive indices. (scale bar: 9 μm) D) The isosurface image of the rendered 3D refractive index distribution after treated FHA-NPs or X-ray irradiation separately or simultaneously. Blue and white represent the refractive indices of the nucleus and cytoplasm, while yellow and red represent the refractive indices of lipid droplets and FHA-NPs, respectively. The image on the right is an enlarged image. E) Mean RI value and F) sphericity of A549 whole cell after treatment in each group. G) Mean RI value, H) sphericity, I) surface area (μm^2), J) volume (μm^3), K) dry mass (pg), and L) concentration of lipid droplets after treatment in each group. *$p < 0.05$, **$p < 0.01$, ***$p < 0.001$.

and volume, the group treated only with X-rays was the most affected. In the rendered 3D refractive index images, we analyzed the mean RI value (Figure 4G), sphericity (Figure 4H), surface area (Figure 4I), volume (Figure 4J), dry mass (Figure 4K), and concentration (Figure 4L) of lipid droplets. Regarding the lipid droplets' refractive index images, the sphericity is the roundness of the 3D lipid droplet; the surface area is the total area of the membrane surrounding a lipid droplet; the volume is the amount of space occupied by a single lipid droplet; and the concentration is the amount of substance present per unit
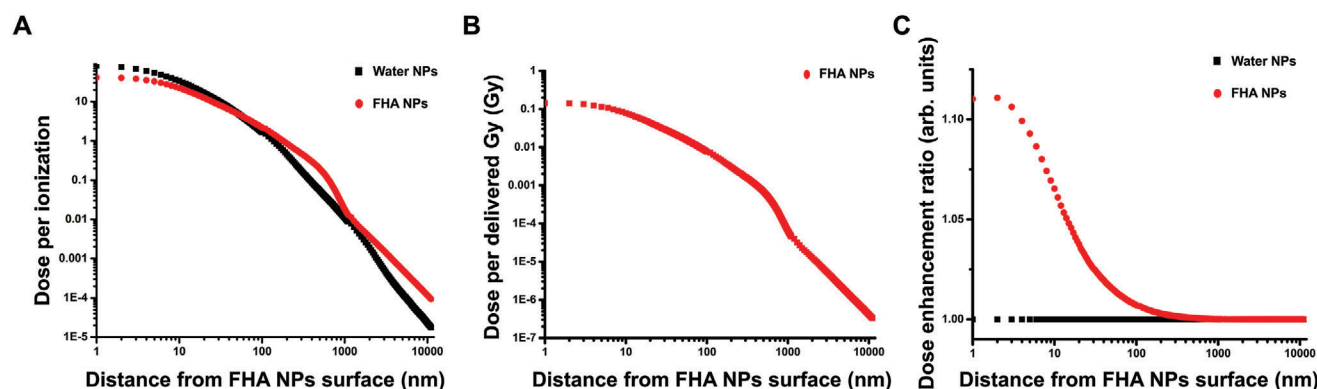
ADVANCED
SCIENCE NEWS
www.advancedsciencenews.com

NANO · MICRO
small
www.small-journal.com

Figure 5. Monte Carlo simulation of the interaction between 300-kVp X-ray irradiation and FHA-NPs located 2 cm away in a water phantom. A) Dose per ionization as a function of the radial distance from the FHA-NP surface. Radial dose distribution as a function from the FHA-NP surface B) per delivered Gy C) per enhancement ratio (DER).

volume of lipid droplets. The correlation of lipid droplets was very high in the separately or simultaneously treatment group with FHA-NPs compared to the control group.[56,57] Lipid droplets play an important role in regulating lipid metabolism, but few studies show direct correlations and results between ferroptosis and lipid droplets. These results can be used for future research on the relationship between ferroptosis and lipid droplets and to clarify related mechanisms. Furthermore, identifying the role of lipid droplets in cancer treatment suggests a new promising research direction to develop novel cancer treatments.

2.4. Monte Carlo Simulation of the Interaction Between FHA-NPs and X-Rays

Monte Carlo simulations were carried out to assess the additional dose deposited because of the presence of FHA-NPs when exposed to 300 kVp X-rays located 2 cm away in the water phantom. **Figure 5A** shows the dose deposited per ionization event produced inside the FHA-NPs. It should be noted that, although the probability of interaction was higher for the FHA-NPs, a water NP with the same dimensions deposited a greater dose in the immediate region of the NP surface. This is explained by a self-absorption effect occurring inside the nanoparticle, which prevents the very low-energy secondary particles from escaping their own volume. Nevertheless, after the first 100 nm, it was the FHA-NPs that deposited a higher amount of dose. Figure 5B shows the radial dose deposited because of interactions with the FHA-NPs after exposure to a 1-Gy dose of X-rays. The interaction probability of the FHA-NPs with 300 kVp X-rays was not radically different from that of water, which implies that, for every delivered Gy, the NPs will deposit an additional ≈0.1 Gy in its close vicinity. In addition, Figure 5C shows that FHA-NPs enhanced the dose by up to 10% in the initial nanometers from the NP surface. However, the dose enhancement rapidly decreased after the first 100 nm of radial distance, denoting that the dose-amplification effect is limited to a significantly short distance from the FHA-NPs. Based on the simulation results; we presumed the radial dose enhancement contributes to cancer cell-killing. Although Fe radio enhancement is limited to a fairly limited distance, a dose increment was appreciated.

2.5. Confirmation of the Therapeutic Effect of the FHA-NP and X-Ray Irradiation Combination In Vivo

To demonstrate the tumor suppression effect of FHA-NPs and combination therapy efficacy with X-ray irradiation, subcutaneous tumors were established in nude mice using A549 cells. We divided the animals into four groups: a control group injected with PBS (Ctrl), a group treated only with FHA-NPs (FHA NPs), a group only irradiated with X-rays (X-ray), and a group treated with FHA-NPs and X-rays simultaneously (FHA NPs + X-ray) (n = 3 mice per group). Moreover, after the implantation of A549 cells, the study was started on day 66, when the average initial tumor volume reached 271 mm^3 (Figure S18, Supporting Information). We administered FHA-NPs (40 mg kg^{-1}) to mice via peritumoral subcutaneous injection around the tumor and irradiated it with a 320-kV X-ray irradiation apparatus. After the administration of FHA-NPs, X-ray irradiation was performed the following day, and FHA-NPs and X-ray irradiation were repeated 9 days later; changes in tumor size were observed after a total of two treatments, respectively (**Figure 6A**). Sacrifice was performed on day 16 after the first FHA-NPs injection, and the survival rate of mice in all groups was 100% (Figure S19, Supporting Information). At the same time, the A375P model was constructed to establish preclinical safety and treatment plans using FHA-NPs composed of safe materials that induce ferroptosis. To further verify the number of injections, dose, and safety of FHA-NPs, an experiment was designed differently from the A549 model, and the dose was set to the maximum by referring to a paper based on iron nanoparticles. A375P cells were used to establish subcutaneous tumors in nude mice and divided into five groups: a control group injected with PBS (Ctrl), a group treated only with FHA-NP twice (2FHA NPs), a group treated with only FHA-NP six times(6 FHA NPs), a group irradiated only with X-rays (X-ray), and a group treated with FHA-NP six times and X-rays simultaneously (6FHA NPs + X-ray) (n = 5 mice per group). Moreover, the study started on day 49 after the implantation of A375P cells, when the average initial tumor volume reached 243 mm^3 (Figure S20, Supporting Information). We administered subcutaneous injection around the tumor in the same way as the A549 model, but the concentration of FHA-NPs was 100 mg kg^{-1}, which is 2.5 times higher than that of the A549 model. The group
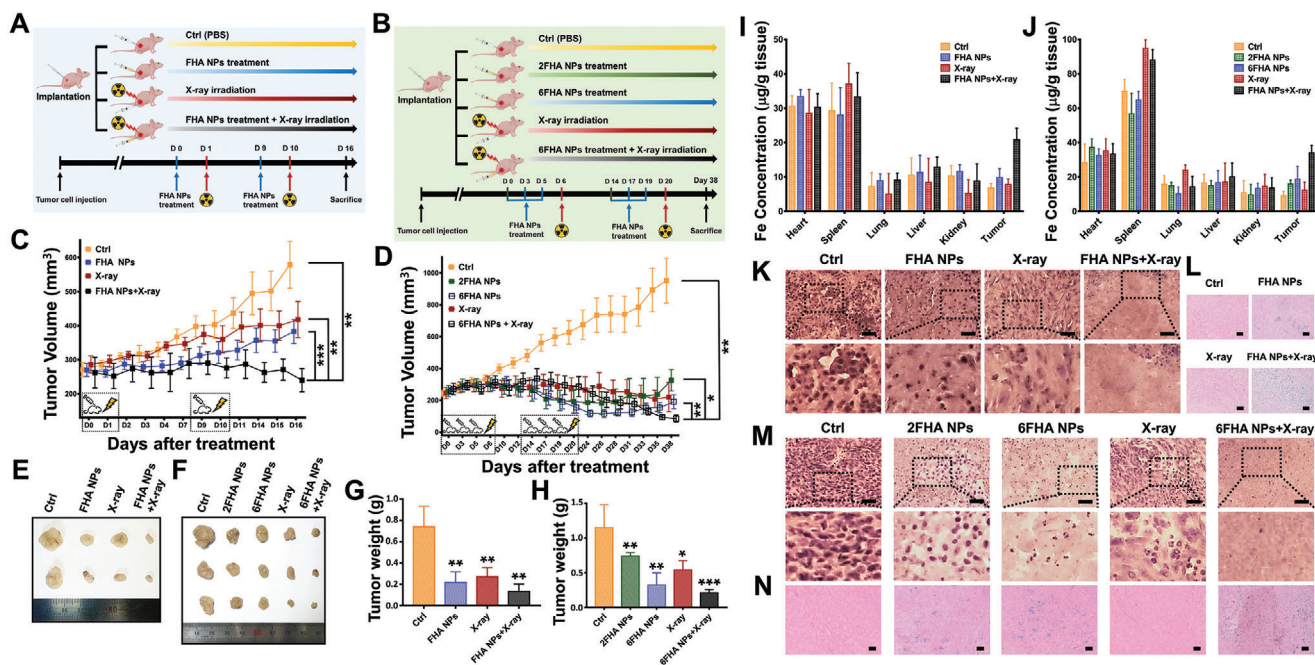
ADVANCED
SCIENCE NEWS

www.advancedsciencenews.com

NANO · MICRO
small
www.small-journal.com

Figure 6. Confirmation of tumor suppression by the combination therapy of FHA-NPs with X-ray irradiation in vivo. A) Schematic diagram of the in vivo treatment strategy in the A549 model. B) Schematic diagram of the in vivo treatment strategy in the A375P model. Tumor volume profiling over time after treatment in the C) A549 and D) A375P models. Photographs of tumor size after the sacrifice of mice in the Ctrl, FHA-NP-treated, X-ray irradiation, and combination groups, respectively, in E) A549 and F) A375P models. Tumor weights in the Ctrl, FHA-NP-treated, X-ray irradiated, and combination therapy groups after mice were sacrificed in G) A549 and H) A375P models. Values are the means ± SD. Biodistribution of FHA-NPs in the heart, spleen, lung, liver, kidney, and tumor of the I) A549 and J) A375P models analyzed by ICP-AES. Values are the means ± SD, n = 3. H&E staining of a tumor section sacrificed in K) A549 and M) A375P models (scale bar, 50 μm). Prussian blue staining images of tumor sections from the Ctrl, FHA-NP-treated, X-ray irradiated, and combination therapy groups in L) A549 and N) A375P models (scale bar, 100 μm). Data are presented as the mean ± SD. $^*p < 0.05$, $^{**}p < 0.01$, $^{***}p < 0.001$.

administered FHA-NPs twice the group and irradiated only with X-rays were treated at two-week intervals, and the group administered FHA-NPs six times was treated three times at two-day intervals and repeated. In the combination treatment group, FHA-NPs were injected three times, and X-rays were taken the next day, and this was repeated a week later (Figure 6B). Sacrifice was performed 38 days after the first FHA-NPs injection, and the survival rate of mice in all groups was 100% even though the tumor suppression effect of the A375P model was much higher than that in the A549 model by injecting a higher dose of FHA-NPs (Figure S21, Supporting Information). The tumor volume of the A549 model, which started at an average of 271 ± 21 mm³, increased to 579 ± 69 mm³ in the Ctrl group on day 16, 383 ± 35 mm³ in the FHA-NP-treated group, 418 ± 53 mm³ in the X-ray-irradiated group, and 240 ± 34 mm³ in the combined treatment group, respectively (Figure 6C; Figure S22, Supporting Information). The tumor volume of the A375 model, which started at an average of 243 ± 20 mm³, increased to 952 ± 141 mm³ in the Ctrl group on day 38, 326 ± 67 mm³ in the 2FHA NPs treatment group, 191 ± 44 mm³ in the 6FHA NPs treatment group, and 220 ± 92 mm³ in the X-ray-treatment group, and 85 ± 22 mm³ in the combined treatment group, respectively (Figure 6D; Figure S23, Supporting Information). The tumor volume reduction rate of the 6FHA NPs group, repeated three times twice, was better than the 2FHA NPs group. After treatment with FHA-NPs, A375P model mice were continuously observed without ad-

ditional treatment, and tumor size tended to increase after 10 days of the last FHA-NPs treatment in both the 2FHA NPs group and the 6FHA NPs group. We observed that the therapeutic effect of FHA-NPs is up to 10 days, and the results suggest that the tumor suppressive effect may be greater as the number of treatments with FHA-NPs increases compared to a single treatment. A treatment plan of continuous additional injection of FHA-NPs at weekly intervals may be effective. We observed a very significant tumor volume suppression effect in the combination treatment group. We treated nanoparticles and high-dose X-rays of 10 Gy only twice to confirm the tumor suppression degree without additional treatment. This suggests that, when applied to actual treatment, a more effective tumor suppression effect can be obtained when combined treatment is performed by increasing the number of injections of FHA-NPs with X-ray treatment until the complete disappearance of the tumor.

In the photos obtained for each tumor in the A549 model in Figure 6E and the A375P model in Figure 6F, the size of the tumor decreased after FHA-NP treatment and X-ray irradiation compared to the Ctrl group, and the size of the tumor decreased significantly after the combination treatment. Moreover, the average tumor weight recorded after A549 model sacrifice was 0.74 ± 0.19 g for the Ctrl, 0.21 ± 0.1 g for the FHA-NP-treated, 0.26 ± 0.08 g for the X-ray-irradiated, and 0.1 ± 0.07 g for the combined treatment groups (Figure 6G). Moreover, the average tumor weight recorded after the sacrifice of the A375P model was

1.15 ± 0.33 g for Ctrl, 0.74 ± 0.05 g for the 2FHA NPs group, 0.32 ± 0.17 g for the 6FHA NPs group, and 0.54 ± 0.13 g for X-ray irradiation, and 0.21 ± 0.05 g for the combined treatment groups (Figure 6H). Next, to determine the extent of intratumoral accumulation and biodistribution of iron, a component of FHA-NPs, in each animal model of A549 (Figure 6I) and A375P models (Figure 6J) through ICP-AES analysis, Fe concentration per gram was measured in various tissues (heart, spleen, lung, liver, kidney, and tumor). In both the A549 and A375P models, the concentrations of Fe per gram in the heart, lung, liver, and kidney of each group were almost similar compared to the Ctrl group, with no significant differences. In addition, the iron content in the spleen was observed to be slightly higher in the X-ray irradiation group and the combination treatment group in both models. The intratumoral iron concentration of the A549 model was 6.79 ± 1.35 µg g^{-1} in the Ctrl group, 9.87 ± 2.53 µg g^{-1} in the FHA NPs group, 7.8 ± 1.59 µg g^{-1} in the X-ray irradiation group, and 20.8 ± 3.38 µg g^{-1} in the combination treatment group. In the A375P model, the iron concentration in the tumor was 9.11 ± 2.52 µg g^{-1} in the Ctrl group, 15.92 ± 2.24 µg g^{-1} in the 2FHA NPs group, 18.67 ± 7.55 µg g^{-1} in the 6FHA NPs group, 12.31 ± 4.6 µg g^{-1} in the X-ray irradiation group, and 34.08 ± 4.32 µg g^{-1} in the combination treatment group. We confirmed higher intratumoral iron accumulation in the FHA-NPs-treated group compared to the Ctrl group. Moreover, in the FHA-NPs and X-ray combination treatment group, the intratumoral iron concentration was confirmed to be significantly higher than that in the group treated with FHA-NPs alone.

Next, we confirmed the histological observations by H&E staining of tumor tissue sections from each group in the A549 (Figure 6K) and A375P models (Figure 6M). Significant differences were observed in the nuclear staining with hematoxylin in each group. Compared with the Ctrl group, the number of nuclei was significantly reduced in the FHA-NP-treated group, and a nucleus spread was remarkably observed in the X-ray-irradiated group, whereas almost no nuclei were observed in the combination treatment group. The irradiated tumor sections and tumor sections treated with FHA-NPs exhibited extensive nuclear damage, whereas most of the nuclei were absent in the combination treatment, confirming that there was a clear synergistic effect in the group that received the combination treatment. As shown in Figure 6L,N, we performed a histological evaluation of tumor tissue sections from the Ctrl, FHA-NP-treated, X-ray-irradiated, and combination therapy groups using Prussian blue staining, which is a reliable method of evaluation of the accumulation and distribution of iron-based FHA-NPs. The group treated with FHA-NPs showed a positive reaction in blue (region enriched in FHA-NPs) after Prussian blue staining, indicating that the FHA-NPs were well infiltrated into the tumor. In the A549 and A375P models, the synergistic effect of tumor treatment was confirmed through the combined treatment of FHA-NPs and X-ray irradiation. Furthermore, to design the treatment method, the injection frequency and dose of FHA-NPs were increased in the A375P model. Despite injecting a very high dose of FHA-NPs, the survival rate of mice was 100%, and the tumor suppression effect was maximized with little effect on other organs. However, excluding the Ctrl group, the gap between groups was very narrow due to the initial high tumor suppression effect, making clear comparison difficult, and this is considered a limitation of the study of the A375P model. Based on the result that the tumor suppressive effect decreases after 10 days of treatment with FHA-NPs and X-rays, we expect the effectiveness of combined treatment with radiation could be maximized through verification of the dose, additional injection frequency, and interval of FHA-NPs in follow-up studies. Combination therapy with ferroptosis-inducing nanoparticles and X-ray irradiation can further improve therapeutic efficacy by radiosensitizing the target cells, causing additional damage to cancer cells and improving overall therapeutic response in biomedical applications. The feasibility of incorporating various biomaterials in cancer therapy is being actively reported,[58,59,60] and our results provide an additional promising approach to improve therapeutic efficacy while minimizing side effects. This study will be a basis for demonstrating the need for combined treatment with ferroptosis and X-rays.

3. Conclusion

We treated tumors with a combination of X-ray irradiation and FHA-NPs (which induce ferroptosis, an iron-dependent type of cell death), and performed Monte Carlo simulations to assess the physical interactions of the X-rays with the iron nanoparticles. In both in vitro and in vivo experiments, we confirmed that the ability to kill cancer cells was significantly increased when the combination treatment was performed. We induced ferroptotic cancer cell death through FHA-NPs, confirmed that apoptosis was induced by DNA damage through X-ray treatment, and studied an increase in the dose deposited in the region located very close to the FHA-NPs. Of note, a significant amount of lipid droplets was confirmed in FHA-NPs-treated cells, confirming that lipid metabolism is important during ferroptosis. These results provide insight into the identification of the role of ferroptosis in X-ray irradiation therapy and the clarification of the correlation and role of radiation and ferroptosis for effective cancer therapy. In addition, the stability and enhanced killing effect of the FHA-NPs, when combined with radiation treatment, may serve as a basis for reducing the side effects that are commonly associated with radiation therapy, as well as for paving the way for a safer X-ray therapy system. The current study confirmed the combined effect of radiation therapy with safe ferroptosis-inducing nanoparticles that are non-toxic and do not use any cross-linking agent, an FDA-approved material, for a clinical trial in mind, and confirmed physical interactions through Monte Carlo simulation. Finally, our research can be applied to the development of promising new anticancer treatment strategies, including cancer nanotechnology, to improve cancer treatment.

4. Experimental Section

Materials: RPMI 1640 (Welgene, Korea); Quanti-LDH PLUS Cytotoxicity Assay Kit (Biomax, Seoul, Korea); crystal violet (Sigma–Aldrich, USA); Live/Dead Viability/Cytotoxicity Kit (Invitrogen, Carlsbad, CA, USA); Click-iT Plus TUNEL Assay Kit (Invitrogen, USA); Comet Assay Kit (Abcam, ab238544); recombinant anti-gamma H2A.X (phospho S139) antibody (Abcam, ab81299); goat anti-rabbit IgG H&L (Alexa Fluor 488) (Abcam, ab150077); Optimum Cutting Temperature compound (OCT) (TCI, Tokyo, Japan); MitoTracker Deep Red FM (Invitrogen); Prussian blue ($C_6Fe_2KN_6 \cdot xH_2O$) (Sigma–Aldrich, USA).

Cell Culture: Human lung carcinoma (A549) cells and human malignant melanoma (A375P) were purchased from the Cell Line Bank (Seoul, Korea) and cultured in RPMI 1640 containing 1% penicillin/streptomycin and 10% fetal bovine serum (FBS).

Clonogenic Assay: Cells were seeded at a density of 2×10^3. Before irradiation, 200 µg mL^{-1} FHA-NPs were treated as a suspension, followed by X-ray irradiation (X-RAD 320, Precision X-ray, 300 kVp, North Branford, CT, USA). The irradiation was made following the procedure established by the TG-61 protocol for radiotherapy and radiobiology. The irradiation was done using a 20×20 field size, a 50 cm source-to-surface distance (SSD), and a 2 mm aluminum filter. Four groups (i.e., control (Ctrl), treated with FHA-NPs, X-ray irradiated, treated with FHA-NPs + X-ray irradiation) were formed and irradiated with X-rays at a dose of 1, 3, and 6 Gray (Gy) (n = 3 per group). Two weeks later, the colonies were fixed with a fixation solution and then stained with 0.05% crystal violet. The survival fraction was calculated using the plating efficiency of the control group, as follows.

$$\text{Plating efficiency} \ (PE) = \frac{\text{The number of counted colonies}}{\text{The number of seeded cells}} \times 100\% \quad (1)$$

$$\text{Survival fraction} \ (SF) = \frac{\text{The number of counted colonies}}{\text{The number of seeded cells} \times PE \text{ of control group}} \times 100\% \quad (2)$$

$$\text{Mean inactivation dose} \ (MID) = \int_0^\infty S(D)\, dD \quad (3)$$

$$\text{Sensitizer Enhancement Ratio} \ (SER) = \frac{MID_{\text{control}}}{MID_{\text{NPs}}} \quad (4)$$

LDH Release: A549 cells (2×10^4) were seeded and divided into four groups: control, FHA-NPs treated (200 µg mL^{-1} concentration), X-ray irradiated (6 Gy), and FHA-NPs treated + X-ray irradiated. The percent of lactate dehydrogenase (LDH) was measured using the Quanti-LDH PLUS Cytotoxicity Assay Kit (Biomax, Seoul, Korea) protocol. The absorbance was read at 490 nm using a microplate reader (Bio Tek Synergy H1, USA).

Live/Dead Assay: After seeding the A549 cells (5×10^4) in a 24-well plate, the experiment was conducted by dividing the groups for treatment with FHA-NPs (200 µg mL^{-1}) and X-ray irradiation (6 Gy), respectively, or simultaneously. At 12 h after X-ray irradiation, calcein AM and ethidium homodimer-1 (EthD-1) were administered and observed. Each group was carried out independently in four replicates.

TUNEL Assay: FHA-NPs (200 µg mL^{-1}) and X-ray irradiation (6 Gy) were respectively or simultaneously administered, and the experiment was performed 12 h later. The TUNEL assay was performed using a Click-iT Plus TUNEL Alexa Fluor 488 Assay Kit according to the manufacturer's instructions, followed by counterstaining with DAPI (for visualization of nuclei) and Alexa Fluor 594 Phalloidin (for cytoskeleton visualization); the results were assessed under a laser scanning microscope. Each group was carried out independently in four replicates.

COMET Assay: The Comet assay was performed using a Comet Assay Kit at 12 h after the onset of the treatment with FHA-NPs (200 µg mL^{-1}) and X-ray irradiation (6 Gy), respectively, or simultaneously. The degree of DNA damage was confirmed via staining with the Vista Green DNA dye, followed by observation under a laser scanning microscope. The percentage of DNA in Comet Tail, tail length, and tail moment were calculated using the CometScore analytical software (CometScore 2.0).

Immunofluorescence Assay: A549 cells (3×10^4) were seeded and treated with FHA-NPs (200 µg mL^{-1}) and X-ray irradiation (6 Gy), separately or simultaneously for 24 h. For permeabilization, 0.1% Triton X-100 in PBS with 1% BSA was administered and the cells were incubated overnight with an anti-gamma H2A.X (Phospho S139; 1:100) antibody at

4 °C. Subsequently, goat anti-rabbit IgG H&L (Alexa Fluor 488) was administered at a dilution of 1:500 for 1 h at room temperature. Each group was carried out independently in four replicates. The results were visualized with a laser scanning microscope and the number of foci per nucleus was calculated using the ImageJ software.

Analysis of Reactive Oxygen Species (ROS): A549 cells (5×10^4) were seeded and cultured overnight, then divided into groups that were treated separately or simultaneously with FHA-NPs (200 µg mL^{-1}) and X-rays (6 Gy) for 12 h. The CellROX orange was added and the results were visualized under a laser scanning microscope. Each group was carried out independently in four replicates.

3D Cell Explorer Imaging: A549 cells (3×10^5) were seeded and treated with FHA-NPs (200 µg mL^{-1}) and X-rays (6 Gy) separately or simultaneously. Twelve hours later, the cells were washed three times, fixed with 4% paraformaldehyde for 30 min, and observed under a 3D super-resolution microscope (3D Cell Explorer, Nanolive, Switzerland).

Optical Diffraction Tomography (ODT): ODT images were acquired 12 h after treatment with FHA-NPs (200 µg mL^{-1}) and X-rays (6 Gy) separately or simultaneously. After staining with DAPI and MitoTracker Deep Red FM, the 3D intracellular localization was observed using a commercially available ODT instrument (HT-1H; Tomocube Inc., Korea), with confirmation achieved by high refractive index (RI) values.

Monte Carlo Simulation: The Monte Carlo simulations were carried out as reported previously by Sung et al. for gold nanoparticles.[61] The simulations were performed using TOPAS 3.8.1, built on GEANT4 10.07. p03.[62] The simulation was divided into three steps. The initial simulation involved a 50-mm water phantom beam irradiated by a 300 kVp photon beam.[63] A 10-mm-radius phase space file, which recorded all passing photons, was located at a depth of 2 cm from the water phantom. Subsequently, the recorded phase space was re-scaled to a diameter of 100 nm, to match the FHA-NPs. A second phase space file scored the secondary electrons produced inside the nanoparticles that were able to escape from them. In the third simulation, the phase space file that scored the electrons that had escaped the FHA-NPs was used as a source beam in a $2.5 \times 2.5 \times 2.5 \ \mu m^3$ water phantom. The radial dose was scored by spherical shells with a thickness ranging from 1 to 100 nm, from 10 nm to 1 µm, and from 100 nm to 10 µm beginning from the FHA-NPs surface at the 50-nm radius from the center of the water phantom. To calculate the dose enhancement factor (DEF), the iron oxide nanoparticle was replaced with the same volume of water (WNP). Replacing the FHA-NPs volume with water is not realistic; however, it will produce sufficient interactions to compare the dose of the secondary particles located in the close vicinity with the nanoparticle volume. The DEF was defined as follows:

$$\text{DEF} \ (r) = \frac{\text{Dose} (r)_{NP} \times \text{Interaction probability}_{NP} + D_{Bg}}{\text{Dose} (r)_{WNP} \times \text{Interaction probability}_{WNP} + D_{Bg}} \quad (5)$$

where Dose (r) is the radial dose per ionization event in the nanoparticle volume containing iron oxide or water, interaction probability is the probability of a single particle from the beam source of hitting and creating an ionization event, and D_{Bg} is the background dose from the primary beam, which was defined as the dose deposited by a single particle in the water phantom. The simulations were performed using Penelope physics for the iron oxide material, whereas Geant4-DNA physics was used for the liquid water.[64–66] The electrons were tracked down to 100 eV and the production threshold was set to 1 nm. Fluorescence, Auger electron emission, and Auger cascades were active throughout all simulations.

Animal Models and Tumor Inoculation: Five-week-old female athymic Balb/c Nude mice (weight, 18 ± 2 g) were supplied by Central Lab. Animal, Inc. A549 cells (1.25×10^6 cells per 100 µL) and A375P (1×10^6 cells per 100 µL) were subcutaneously injected. FHA-NPs (40 mg kg^{-1} per 50 µL) were administered to the mice via peritumoral subcutaneous injection for the A549 model and FHA-NPs (100 mg kg^{-1} per 50 µL) were administered to the mice via peritumoral subcutaneous injection for A375P model (Department of Laboratory Animal Resources, Yonsei Biomedical Research Institute, Yonsei University College of Medicine, Seoul, Korea), (IACUC Permit Number: AEC-20080529-0001). Tumor growth was confirmed by

**ADVANCED
SCIENCE NEWS**

www.advancedsciencenews.com

NANO · MICRO
small

www.small-journal.com

measuring the vertical diameter width and length, respectively, and tumor volume was calculated using the following equation: Tumor volume = $\frac{1}{2}(\text{Width}^2 \times \text{Length})$.

Radiation System Step: Prior to X-ray irradiation, the mice were anesthetized with isoflurane and immobilized on the platform using surgical tape. For all irradiation treatments, a 320-kVp X-ray irradiation apparatus (X-Rad320, Precision, USA) was used according to the experimental setting (dose, 10 Gy; dose rate; 1.65 cGy min^{-1}).

Fe Quantification in Organs via ICP-AES: Organ and tumor samples were weighed and digested with a mixture of concentrated nitric acid and hydrogen peroxide at a volume ratio of 4:1. Samples were processed on a hot plate at 120 °C for 30 min and then at 83 °C for an additional 6 h. Transfer to a new tube and bring the total volume to 10 mL with ultrapure water. Each sample was repeated three times and measured by inductively coupled plasma-atomic emission spectroscopy (ICP-AES) (Optima 8300; Perkin-Elmer, USA).

Histological Analysis: Tumors were fixed with 4% formaldehyde and saturated with increasing concentrations of sucrose in PBS. Subsequently, cryosections were prepared at a thickness of 10 μm and used for tissue staining.

Prussian Blue and H&E Staining: Tissues were stained with Prussian blue and counterstained with nuclear fast red for Prussian blue staining. After washing, the tissue was dehydrated with alcohol, and examined under a laser scanning microscope. H&E staining was performed using a Hematoxylin and Eosin (H&E) staining kit, according to the manufacturer's instructions.

Statistical Analysis: The analyses were performed using the GraphPad Prism software (Graph-Pad Software, Inc., USA) and the figures were created using BioRender (agreement number TA25AJ2DF7). Statistical significance was evaluated using one-way ANOVA with Tukey's test, and the significance of differences was set at $^*p < 0.05$.

Supporting Information

Supporting Information is available from the Wiley Online Library or from the author.

Conflict of Interest

The authors declare no conflict of interest.

Data Availability Statement

The data that support the findings of this study are available in the supplementary material of this article.

[1] S. N. Bhatia, X. Chen, M. A. Dobrovolskaia, T. Lammers, *Nat. Rev. Cancer* **2022**, *22*, 550.
[2] J. Shi, P. W. Kantoff, R. Wooster, O. C. Farokhzad, *Nat. Rev. Cancer* **2017**, *17*, 20.
[3] M. J. Nirmala, U. Kizhuveetil, A. Johnson, G. Balaji, R. Nagarajan, V. Muthuvijayan, *RSC Adv.* **2023**, *13*, 8606.
[4] J. A. Kemp, Y. J. Kwon, *Nano Convergence* **2021**, *8*, 34.
[5] Z. Cheng, M. Y. Li, R. Dey, Y. H. Chen, *J. Hematol. Oncol.* **2021**, *14*, 85.
[6] D. Rosenblum, N. Joshi, W. Tao, J. M. Karp, D. Peer, *Nat. Commun.* **2018**, *9*, 1410.
[7] P. N. Navya, A. Kaphle, S. P. Srinivas, S. K. Bhargava, V. M. Rotello, H. K. Daima, *Nano Convergence* **2019**, *6*, 1.
[8] I. Dagogo-Jack, A. T. Shaw, *Nat. Rev. Clin. Oncol.* **2018**, *15*, 81.
[9] P. J. Wu, W. Gao, M. Su, E. C. Nice, W. H. Zhang, J. Lin, N. Xie, *Front Cell Dev Biol* **2021**, *9*, 641469.
[10] R. A. Sharma, R. Plummer, J. K. Stock, T. A. Greenhalgh, O. Ataman, S. Kelly, R. Clay, R. A. Adams, R. D. Baird, L. Billingham, S. R. Brown, S. Buckland, H. Bulbeck, A. J. Chalmers, G. Clack, A. N. Cranston, L. Damstrup, R. Ferraldeschi, M. D. Forster, J. Golec, R. M. Hagan, E. Hall, A.-R. Hanauske, K. J. Harrington, T. Haswell, M. A. Hawkins, T. Illidge, H. Jones, A. S. Kennedy, F. Mcdonald, et al., *Nat. Rev. Clin. Oncol.* **2016**, *13*, 627.
[11] S. T. Yu, Y. Wang, P. He, B. F. Shao, F. Liu, Z. Z. Xiang, T. Yang, Y. Y. Zeng, T. He, J. C. Ma, X. R. Wang, L. Liu, *Front Oncol* **2022**, *12*, 809304.
[12] S. J. Dixon, K. M. Lemberg, M. R. Lamprecht, R. Skouta, E. M. Zaitsev, C. E. Gleason, D. N. Patel, A. J. Bauer, A. M. Cantley, W. S. Yang, B. Morrison, B. R. Stockwell, *Cell* **2012**, *149*, 1060.
[13] K. Salnikow, *Semin. Cancer Biol.* **2021**, *76*, 189.
[14] Y. Chen, Z. M. Fan, Y. Yang, C. Y. Gu, *Int J Oncol* **2019**, *54*, 1143.
[15] Q. Q. Guo, L. W. Li, S. S. Hou, Z. Q. Yuan, C. H. Li, W. Z. Zhang, L. F. Zheng, X. M. Li, *Front Oncol* **2021**, *11*, 778492.
[16] S. V. Torti, F. M. Torti, *Nat. Rev. Cancer* **2013**, *13*, 342.
[17] C. G. Zhang, F. Zhang, *Protein & Cell* **2015**, *6*, 88.
[18] C. Bae, H. Kim, Y. M. Kook, C. Lee, C. Kim, C. Yang, M. H. Park, Y. Z. Piao, W. G. Koh, K. Lee, *Mater Today Bio* **2022**, *17*, 100457.
[19] X. Gao, J. Feng, K. H. Lv, Y. F. Zhou, R. H. Zhang, S. Y. Song, H. J. Zhang, D. G. Wang, *Nano Res.* **2023**, *16*, 9826.
[20] Y. Q. Wang, J. Chen, J. X. Lu, J. Q. Xi, Z. L. Xu, L. Fan, H. Dai, L. Z. Gao, *J. Nanobiotechnol.* **2022**, *20*, 199.
[21] Z. Yang, A. Yang, W. Ma, K. Ma, Y.-K. Lv, P. Peng, S.-Q. Zang, B. Li, *J. Nanobiotechnol.* **2022**, *20*, 1.
[22] M. Yu, J. Yu, Y. Yi, T. Chen, L. Yu, W. Zeng, X.-K. Ouyang, C. Huang, S. Sun, Y. Wang, Y. Liu, C. Lin, M. Wu, L. Mei, *J. Controlled Release* **2022**, *347*, 104.
[23] C. Xie, T. Zhang, Y. Fu, G. Han, X. Li, *Nano Res.* **2022**, *15*, 8281.
[24] R. Baskar, K. A. Lee, R. Yeo, K.-W. Yeoh, *Int J Med Sci* **2012**, *9*, 193.
[25] H. Nakano, K. Shinohara, *Radiat. Res.* **1994**, *140*, 1.
[26] H. Zhao, Y. F. Zhuang, R. B. Li, Y. Y. Liu, Z. J. Mei, Z. S. He, F. X. Zhou, Y. F. Zhou, *Oncol Lett* **2019**, *17*, 42.
[27] G. Lei, Y. Zhang, P. Koppula, X. Liu, J. Zhang, S. H. Lin, J. A. Ajani, Q. Xiao, Z. Liao, H. Wang, B. Gan, *Cell Res.* **2020**, *30*, 146.

[28] L. F. Ye, K. R. Chaudhary, F. Zandkarimi, A. D. Harken, C. J. Kinslow, P. S. Upadhyayula, A. Dovas, D. M. Higgins, H. Tan, Y. Zhang, M. Buonanno, T. J. C. Wang, T. K. Hei, J. N. Bruce, P. D. Canoll, S. K. Cheng, B. R. Stockwell, *ACS Chem. Biol.* **2020**, *15*, 469.

[29] G. Lei, C. Mao, Y. L. Yan, L. Zhuang, B. Y. Gan, *Protein & Cell* **2021**, *12*, 836.

[30] Y. Shibata, H. Yasui, K. Higashikawa, N. Miyamoto, Y. Kuge, *PLoS One* **2019**, *14*, e0225931.

[31] J. Su, C. Bian, Z. Zheng, H. Wang, L. Meng, Y. Xin, X. Jiang, *Front Cell Dev Biol* **2022**, *10*, 951116.

[32] X. Lang, M. D. Green, W. Wang, J. Yu, J. E. Choi, L. Jiang, P. Liao, J. Zhou, Q. Zhang, A. Dow, A. L. Saripalli, I. Kryczek, S. Wei, W. Szeliga, L. Vatan, E. M. Stone, G. Georgiou, M. Cieslik, D. R. Wahl, M. A. Morgan, A. M. Chinnaiyan, T. S. Lawrence, W. Zou, *Cancer Discov* **2019**, *9*, 1673.

[33] Y. Lin, X. Chen, C. Yu, G. Xu, X. Nie, Y. Cheng, Y. Luan, Q. Song, *Acta Biomater.* **2023**, *159*, 300.

[34] Y.-K. Hou, Z.-J. Zhang, R.-T. Li, J. Peng, S.-Y. Chen, Y.-R. Yue, W.-H. Zhang, B. Sun, J.-X. Chen, Q. Zhou, *ACS Appl. Mater. Interfaces* **2023**, *15*, 2602.

[35] W. Jiang, L. Wei, B. Chen, X. Luo, P. Xu, J. Cai, Y. Hu, *J Nanobiotechnology* **2022**, *20*, 129.

[36] H. Sun, H. Cai, C. Xu, H. Zhai, F. Lux, Y. Xie, L. Feng, L. Du, Y. Liu, X. Sun, Q. Wang, H. Song, N. He, M. Zhang, K. Ji, J. Wang, Y. Gu, G. Leduc, T. Doussineau, Y. Wang, Q. Liu, O. Tillement, *J. Nanobiotechnol.* **2022**, *20*, 449.

[37] A. P. Klapproth, J. Schuemann, S. Stangl, T. W. Xie, W. B. Li, G. Multhoff, *Cancer Nanotechnol.* **2021**, *12*, 27.

[38] A. D. Paro, M. Hossain, T. Webster, M. Su, *Int. J. Nanomed.* **2016**, *11*, 4735.

[39] A. Gayol, F. Malano, C. R. Montenovo, P. Perez, M. Valente, *Int. J. Mol. Sci.* **2023**, *24*, 514.

[40] S. Rajabpour, H. Saberi, J. Rasouli, N. Jabbari, *Sci. Rep.* **2022**, *12*, 1779.

[41] N. A. P. Franken, H. M. Rodermond, J. Stap, J. Haveman, C. Van Bree, *Nat. Protoc.* **2006**, *1*, 2315.

[42] K. Buch, T. Peters, T. Nawroth, M. Sanger, H. Schmidberger, P. Langguth, *Radiation Oncology* **2012**, *7*, 1.

[43] N. Brix, D. Samaga, R. Hennel, K. Gehr, H. Zitzelsberger, K. Lauber, *Radiation Oncology* **2020**, *15*, 1.

[44] C. Legrand, J. M. Bour, C. Jacob, J. Capiaumont, A. Martial, A. Marc, M. Wudtke, G. Kretzmer, C. Demangel, D. Duval, J. Hache, *J. Biotechnol.* **1992**, *25*, 231.

[45] Z. Darzynkiewicz, D. Galkowski, H. Zhao, *Methods* **2008**, *44*, 250.

[46] K. Kyrylkova, S. Kyryachenko, M. Leid, C. Kioussi, *Methods Mol Biol* **2012**, *887*, 41.

[47] H. F. Yan, T. Zou, Q. Z. Tuo, S. Xu, H. Li, A. A. Belaidi, P. Lei, *Signal Transduct Target Ther* **2021**, *6*, 49.

[48] B. R. Stockwell, *Free Radic Biol Med* **2018**, *120*, S7.

[49] Y. Cheng, Y. Song, H. Chen, Q. Li, Y. Gao, G. Lu, C. Luo, *Oxid Med Cell Longev* **2021**, *2021*, 5005136.

[50] S. V. Kostyuk, E. V. Proskurnina, M. S. Konkova, M. S. Abramova, A. A. Kalianov, E. S. Ershova, V. L. Izhevskaya, S. I. Kutsev, N. N. Veiko, *Int. J. Mol. Sci.* **2022**, *23*, 261.

[51] K. Kawamura, F. Qi, J. Kobayashi, *J Radiat Res* **2018**, *59*, ii91.

[52] M. Gao, J. Yi, J. Zhu, A. M. Minikes, P. Monian, C. B. Thompson, X. Jiang, *Mol. Cell* **2019**, *73*, 354.

[53] A. M. Battaglia, R. Chirillo, I. Aversa, A. Sacco, F. Costanzo, F. Biamonte, *Cells* **2020**, *9*, 1505.

[54] K. Kaminaga, R. Hamada, N. Usami, K. Suzuki, A. Yokoya, *Radiat. Res.* **2020**, *194*, 511.

[55] D. W. M. Walsh, C. Siebenwirth, C. Greubel, K. Ilicic, J. Reindl, S. Girst, G. Muggiolu, M. Simon, P. Barberet, H. Seznec, H. Zischka, G. Multhoff, T. E. Schmid, G. Dollinger, *Sci Rep.* **2017**, *7*, 46684.

[56] D. Kim, S. Lee, M. Lee, J. Oh, S. A. Yang, Y. Park, *Advanced Imaging and Bio Techniques for Convergence Science* **2021**, *1310*, 211.

[57] T. A. Stanly, R. Suman, G. F. Rani, P. J. O'Toole, P. M. Kaye, I. S. Hitchcock, *Front Physiol* **2020**, *11*, 568087.

[58] R. Khalilov, *Adv. Biol. Earth Sci.* **2023**, *8*, 1.

[59] A. Eftekhari, C. Kryschi, D. Pamies, S. Gulec, E. Ahmadian, D. Janas, S. Davaran, R. Khalilov, *Nanotheranostics* **2023**, *7*, 236.

[60] E. Ahmadian, D. Janas, A. Eftekhari, N. Zare, *Chemosphere* **2022**, *302*, 134826.

[61] W. Sung, S.-J. Ye, A. L. Mcnamara, S. J. Mcmahon, J. Hainfeld, J. Shin, H. M. Smilowitz, H. Paganetti, J. Schuemann, *Nanoscale* **2017**, *9*, 11338.

[62] J. Perl, J. Shin, J. Schümann, B. Faddegon, H. Paganetti, *Med Phys* **2012**, *39*, 6818.

[63] G. Poludniowski, G. Landry, F. Deblois, P. M. Evans, F. Verhaegen, *Phys Med Biol* **2009**, *54*, N433.

[64] S. Incerti, I. Kyriakou, M. A. Bernal, M. C. Bordage, Z. Francis, S. Guatelli, V. Ivanchenko, M. Karamitros, N. Lampe, S. B. Lee, S. Meylan, C. H. Min, W. G. Shin, P. Nieminen, D. Sakata, N. Tang, C. Villagrasa, H. N. Tran, J. M. C. Brown, *Med Phys* **2018**, *45*, E722.

[65] M. A. Bernal, M. C. Bordage, J. M. C. Brown, M. Davídková, E. Delage, Z. El Bitar, S. A. Enger, Z. Francis, S. Guatelli, V. N. Ivanchenko, M. Karamitros, I. Kyriakou, L. Maigne, S. Meylan, K. Murakami, S. Okada, H. Payno, Y. Perrot, I. Petrovic, Q. T. Pham, A. Ristic-Fira, T. Sasaki, V. Stépán, H. N. Tran, C. Villagrasa, S. Incerti, *Physica Medica-European Journal of Medical Physics* **2015**, *31*, 861.

[66] S. Incerti, A. Ivanchenko, M. Karamitros, A. Mantero, P. Moretto, H. N. Tran, B. Mascialino, C. Champion, V. N. Ivanchenko, M. A. Bernal, Z. Francis, C. Villagrasa, G. Baldacchino, P. Guèye, R. Capra, P. Nieminen, C. Zacharatou, *Med Phys* **2010**, *37*, 4692.